Available online at www.sciencedirect.com
SCIENCE DIRECT
Acta Materialia 54 (2006) 4079–4089
Acta MATERIALIA
www.actamat-journals.com

# Microstructure and mechanical properties of super-strong nanocrystalline tungsten processed by high-pressure torsion

Q. Wei [a,*], H.T. Zhang [b], B.E. Schuster [b,c], K.T. Ramesh [b], R.Z. Valiev [d], L.J. Kecskes [c], R.J. Dowding [c], L. Magness [c], K. Cho [c]

[a] Department of Mechanical Engineering, University of North Carolina at Charlotte, Charlotte, NC 28223-0001, USA
[b] Center for Advanced Ceramic and Metallic Systems (CAMCS), Johns Hopkins University, Baltimore, MD 21218, USA
[c] US Army Research Laboratory, Aberdeen Proving Ground, MD 21005, USA
[d] Ufa State Aviation Technical University, Ufa 450000, Russia

Received 8 December 2005; received in revised form 25 April 2006; accepted 2 May 2006
Available online 14 July 2006

**Abstract**

Fully dense nanocrystalline tungsten (nc-W) with extremely high strength (~3.0 GPa under quasi-static compression and ~4.0 GPa under dynamic compression) has been obtained by high-pressure torsion (HPT) at low temperature (500 °C). The nanocrystalline microstructure is revealed by transmission electron microscopy (TEM). The grain boundaries (GBs) are mostly of the large-angle type. High-resolution TEM (lattice images) suggests that the GBs are clean and well defined (atomically sharp). GBs are non-equilibrium and of a high-energy nature. Edge dislocations are present within the grains. The authors hypothesize that these edge dislocations, combined with a depleted impurity concentrations along pre-existing GBs, contribute to enhance the ductility of nc-W. Under dynamic compression, the specimens exhibit localized shearing followed by cracking and subsequent failure, similar to their ultrafine-grain (UFG) counterparts processed by equal-channel angular pressing plus cold rolling, and to many other body-centered cubic metals with UFG/nanocrystalline microstructures. The shear band width in the HPT-processed nc-W is much smaller (shear band width <5 μm) than that observed in the UFG counterparts (shear band width ~40 μm).


*Keywords:* Nanocrystalline; Tungsten; Grain boundaries; Transmission electron microscopy; High-pressure torsion

## 1. Introduction

Due to the various unique properties of materials with nanocrystalline (nc) microstructure (grain size $d <$ 100 nm), tremendous effort has been invested in recent years to the processing and characterization of such materials [1–3]. Several processing techniques have been applied to obtain metals and alloys with ultrafine-grain (UFG, 100 nm $< d \lesssim$ 500 nm) or nc microstructures, including electrodeposition [2,4], powder metallurgy [3,5], inert gas condensation followed by consolidation of powders [2] and severe plastic deformation (SPD) [6,7]. SPD is a "one-step" procedure that starts with a bulk work piece with coarse-grained microstructure and refines the grain size down into the UFG or nc regime with increased plastic straining. SPD provides cost-effective and contamination-free technology for the production of bulk UFG/nc metals and alloys. It has a number of variants, such as equal-channel angular pressing (ECAP) [7], surface mechanical attrition (SMA) [8] and high-pressure torsion (HPT) [9]. HPT has been less investigated than ECAP, and has been applied to a limited number of metals (e.g., Cu, Ni, Fe) [9–11].

It is extremely difficult to produce fully dense, bulk forms with UFG/nc microstructure of some refractory transition metals (typically body-centered cubic (bcc)) that have high melting points and are very susceptible to interstitial

* Corresponding author. Tel.: +1 704 687 8213; fax: +1 704 687 8345.
*E-mail address:* qwei@uncc.edu (Q. Wei).

1359-6454/$30.00 
doi:10.1016/j.actamat.2006.05.005

impurities. Tungsten is the most noticeable example. Conventional coarse-grained tungsten (cg-W) is well known for its poor ductility and high ductile-to-brittle transition temperature (DBTT) [12–14]. At room temperature, cg-W behaves like a ceramic: a strong tension–compression asymmetry, tensile failure without any ductility and, at a stress level only half of the compression "flow" stress, a failure mechanism typical of most brittle ceramics (intergranular fracture). Its high susceptibility to soluble interstitial impurities has been held responsible for such behavior. Those impurities segregate along the grain boundaries (GBs) and render the GBs the weak links during mechanical straining. Some investigations have demonstrated that SPD in the form of ECAP or ECAP followed by low-temperature rolling is a promising technique for the grain size refinement of W to at least UFG level [15–17]. Such microstructure not only increases the strength of W, but also reinstates its ductility. Under dynamic loading, UFG-W exhibits the long sought-after behavior: localized shearing, which is a desirable deformation mode for a number of critical applications [15,16].

We have investigated the microstructure (grain size, grain boundaries, etc.) and mechanical properties, particularly the dynamic failure, of nc-W, processed by low-temperature HPT. Here, low temperature means low homologous temperature, i.e. $T/T_m < 0.25$, where $T_m$ is the melting point in kelvin. Detailed microstructural analyses were performed using conventional transmission electron microscopy (TEM) and high-resolution lattice imaging (HRTEM). The nature of the grain boundaries and the defects within the grains were studied in detail. Quasi-static compression was conducted at various strain rates with specimens from different locations with respect to the center of the HPT W disk. Dynamic uniaxial compression was performed using an innovative desk-top Kolsky bar (or split Hopkinson pressure bar) system [18] which enabled us to test small samples (<1.0 mm) at high strain rates ($\sim 10^3$ to $10^4\ s^{-1}$). We examined the surfaces of the tested specimens for evidence of shear localization using both optical microscopy and scanning electron microscopy (SEM). The fractographic features of some failed specimens were investigated using SEM.

## 2. Experimental

### 2.1. HPT

The starting cg-W of commercial purity was supplied by Plansee (Austria). Table 1 shows the results of chemical analyses on the substitutional and interstitial impurities of the starting material. Initial disk-shaped W billets 9 mm in diameter and 2 mm in thickness were upset by 30% strain at 600 °C in a protective cover to reduce possible oxidation. (Oxidation of W in open air becomes severe at >650 °C [13], the oxide having a yellowish appearance.) Five turns of HPT were performed on the upset and electrochemically polished disk-shaped W using Bridgman anvils pre-heated to 500 °C under an imposed pressure of about 4 GPa. After HPT, no apparent change in color of the W piece was observed, suggesting no serious oxidation of the sample during HPT. To obtain HPT W with thickness <1.0 mm, the lower anvil had a groove 1.0 mm deep and 11.0 mm in diameter. The use of anvils of such a design enables one to obtain samples of about 1.0 mm in thickness and 11.0 mm in diameter without any cracks. Schematic illustrations of HPT can be found in, e.g., Refs. [7,9]. Since the HPT temperature is far below the melting point of W (3695 K, or 3422 °C), and also much below the recrystallization temperature of plastically deformed W (~1250 °C [14,19]), we expect effective microstructure refinement by this SPD route. Two W disks were processed under identical conditions. The von Mises equivalent strain pumped into the work piece is [9]

$$\varepsilon_{vM} = \frac{2\pi N r}{\sqrt{3}h} \tag{1}$$

where $N$ is the number of HPT turns, $r$ is the distance from the center of the disk and $h$ is the thickness of the disk (assuming strict confinement of the disk, no slippage between the W disk and the anvil and thus no thickness reduction during HPT). As an example, if a disk of 10 mm (diameter) × 1.0 mm (thickness) is subjected to one complete turn of HPT, the von Mises equivalent strain experienced by the rim of the disk will be >18. Thus for the HPT W studied in this work, after five HPT turns the maximum nominal strain is about 90!

### 2.2. Microstructural analyses

First, we used X-ray diffraction (XRD) to analyze the HPT W disks for the volume average grain size and internal microstrains. XRD was performed using a Philips X'Pert XRD machine running at 45 kV and 40 A. We conducted segmented scanning to collect XRD data from individual reflections using a step size of $0.01\ s^{-1}$, and a count time of 15 s. The $2\theta$ range was spread to about 4° around the Bragg angle for a given low $\{hkl\}$ family. Therefore the scanning of each peak lasted for about 2 h. We used single line profile analysis [20] to estimate the grain size (or coherent domain size) and microstrains of the samples. The grain size results were compared with TEM observations.

Table 1
Chemical composition of the starting commercial-purity W

| Element | H | O | N | C | S | Al | Ca | Cu | Fe | Mn | Na | Ni |
|---|---|---|---|---|---|---|---|---|---|---|---|---|
| Content (wt.%) | 0.0001 | 0.25 | <0.001 | 0.006 | <0.001 | 0.0010 | 0.0017 | 0.012 | 0.0014 | 0.0008 | 0.0011 | 0.0006 |

TEM specimens were cut from the disks in such a way that the electron beams were in the plane of the disks. The specimens were first mechanically polished from ~0.7 mm down to ~50 μm. Then a dimple was made on the polished specimen. The dimpled specimen was mounted onto a support grid made of tantalum. Electron transparency was achieved by ion milling. A Philips EM420 electron microscope operated at 120 kV was used for conventional TEM analyses. A Philips CM-300 electron microscope operated at 300 kV was used for high-resolution (lattice imaging) TEM. A Gatan digital imaging system recorded the lattice images.

### 2.3. Mechanical testing

We used an MTS servohydraulic loading system to perform uniaxial quasi-static compression (strain rate $10^{-3}$–$10^{0}$ $s^{-1}$). The crosshead speed controlled the strain rate. Because of the limited dimension of the specimens, we conducted dynamic uniaxial compression using a desk-top Kolsky bar [18] (DTKB) system. A schematic of the DTKB set-up is displayed in Fig. 1. The elastic bars carrying the elastic stress waves were made of high-strength maraging steel. The diameter of the bars was ~3.18 mm. Because of the high strength of HPT W, WC platens must be used to protect the elastic bars from plastic yielding. To realize this, impedance-matched WC platens were shrink-fitted into Ti–6Al–4V collars (the outside diameter of the collar was the same as the diameter of the elastic bars). The HPT W specimen (~0.8 mm × 0.8 mm × 1.0 mm) was first sandwiched between two WC platens, and together they were then sandwiched between the input and output bars. The interfaces between the specimen and WC platens were carefully lubricated to minimize friction. The input and output bars and their supports were seated on a precision optical table about 600 mm long. A special alignment procedure had to be performed to ensure the coaxiality of the bars. Strain gages were cemented on the elastic bars to measure (i) the incident pulse generated by an impacting projectile (arriving at the input bar from the right in Fig. 1); (ii) the reflected pulse from the input bar/specimen interface and (iii) the pulse transmitted through the specimen to the output bar. A momentum trap (see Fig. 1; a bar made of the same material and with the same diameter as the input and output bars) was used to protect the strain gage on the output bar. Details of the Kolsky bar technique can be found in Ref. [21].

The side faces of the HPT W specimens were polished to a mirror finish. Specimens were recovered for post-loading examinations for evidence of localized shearing, and for the investigation of dynamic failure, using both optical microscopy and SEM.

## 3. Results

In this section, we first present the results of grain size and microstrain measurement obtained via XRD line broadening analyses. This is followed by detailed TEM observations: from both diffraction contrast and phase contrast (high-resolution lattice imaging). Finally, we provide the results of mechanical testing under uniaxial quasi-static and dynamic compression.

### 3.1. Microstructure of HPT-processed nc-W

First, one of the HPT-processed nc-W (referred to as HPT-W) disks was polished and etched using a standard Murakami solution, and the specimen was examined using an optical microscope at the highest possible magnification. The fine microstructure exceeded the resolution limit of the optical microscope.

For XRD single line profile analysis of grain size (or coherent domain size), first the instrumental broadening was measured using annealed powder of Ni. Our XRD single line profile analyses of the HPT-W result in a volume average coherent domain size of ~40 nm, and a volume average microstrain of ~0.003. We should point out that due to the microstructure gradient in the HPT-W disk plane which is more or less intrinsic to HPT-processed metals [9], these XRD values of grain size and microstrain can

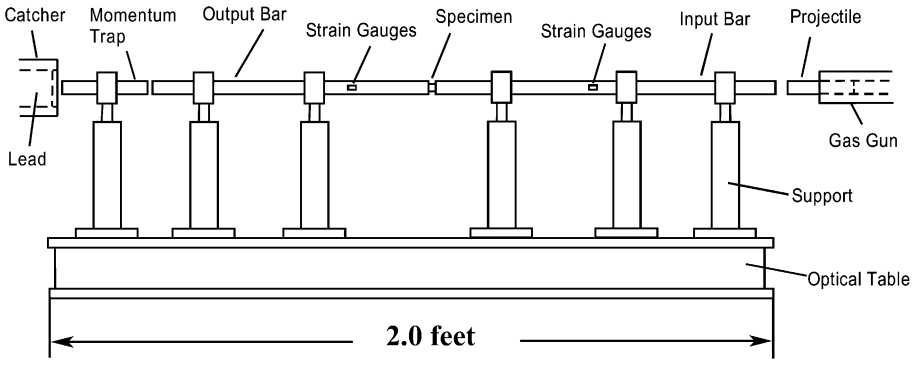


Fig. 1. Schematic of the DTKB system. The bars and their many supports are seated on a precision optical table (~600 mm in length). The bars are made of high-strength maraging steel. The diameter of the bars is ~3.18 mm. The specimen is sandwiched between the input and the output bars. Due to the unusual high strength of the HPT-W, we used impedance-matched WC platens shrink fitted into Ti–6Al–4V collars to protect the input and output bars. Thus the specimen is first sandwiched between the WC platens and then mounted between the two bars.

at most serve as a reference. Later in this paper we will also show that the volume average grain size from XRD analyses is about four times smaller than obtained with TEM analyses. Other authors have also investigated this discrepancy, and it seems to be universal for SPD metals [22].

Fig. 2(a) displays a bright-field TEM micrograph showing the microstructure of HPT-W (nominal HPT equivalent strain ~70). The grains have an elongated shape and a distribution of size. Many grains are heavily dislocated. Break-ups of the elongated grains are apparent. The dark-field image (Fig. 2(b)) also indicates break-ups within the elongated grains. The width of the elongated grains is about 100 nm. Fig. 2(c) shows a selected area electron diffraction (SAED) pattern from the region of Fig. 2(a) and (b). Even though the bright- and dark-field micrographs show elongated morphology, SAED does not suggest strong texturing, as supported by the apparent absence of concentrated intensity in the ring pattern. Instead, the ring pattern from such a small area suggests absence of texturing, and break-ups within the apparently elongated grains. It also suggests that the GBs are mostly of large-angle type, since otherwise concentrated intensity in the ring pattern would be observed. Fig. 3(a) shows yet another bright-field TEM micrograph showing the elongated grains in the HPT-W, with Fig. 3(b) showing the corresponding dark-field image and Fig. 3(c) the diffraction pattern. Again, break-ups in the elongated grains are obvious. Also observed is the sharpness of the GBs, both in the bright-field and dark-field images. We can also take this sharpness as evidence for the large-angle nature of the GBs. HRTEM images in the following will show that those GBs are atomically sharp and well defined.

Fig. 4(a) shows a bright-field digital TEM image showing grains and GBs, and the very small grain size of the HPT-W. We will present high-resolution lattice images of the GB indicated by the rectangular box. Fig. 4(b) shows an HRTEM image of a portion of the GB. The GB is atomically sharp, is of the large-angle type and is clean. No

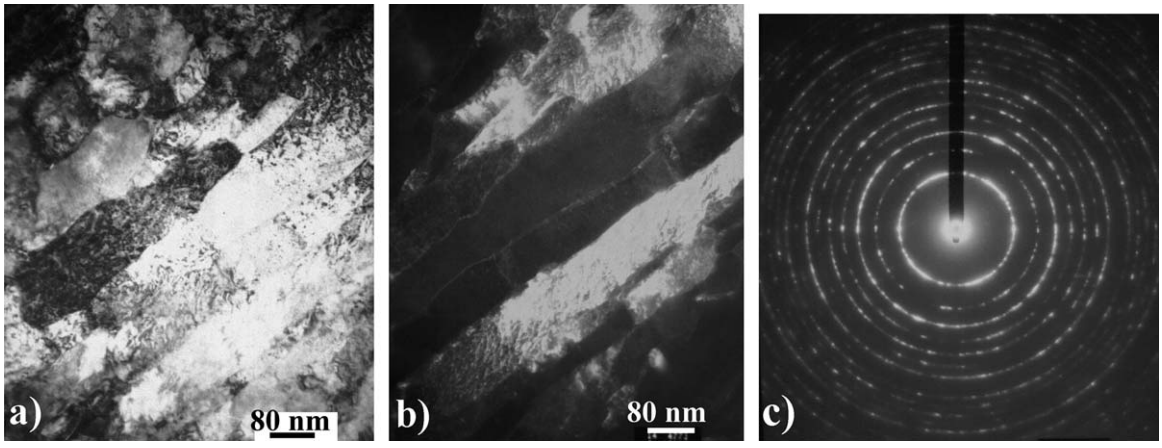


Fig. 2. Bright-field (a), dark-field (b) images and SAED (c) from HPT-W. Notice the high density of defects in the grains, and break-ups in the elongated grains. The SAED shows nearly continuous rings, with no obvious intensity concentration along the rings, indicating large-angle GBs. The HPT nominal equivalent strain in the specimen is around 70.

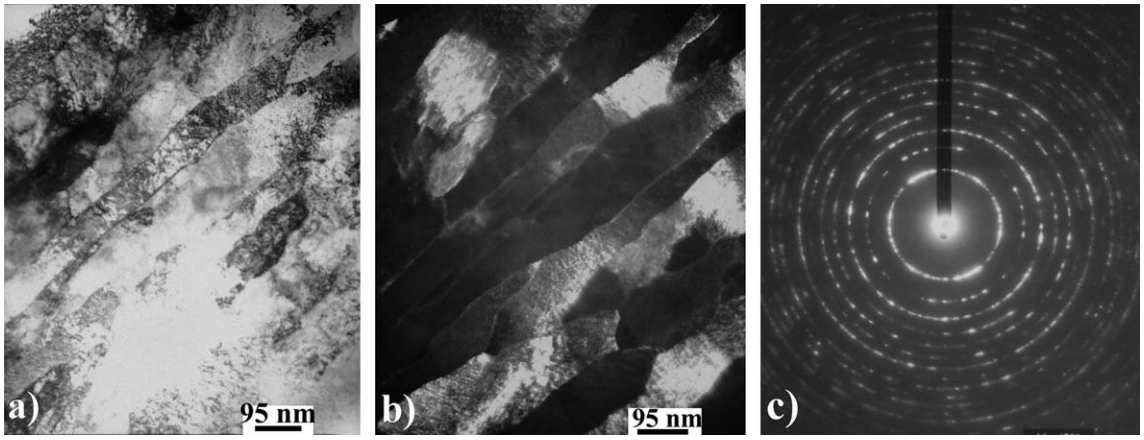


Fig. 3. Bright-field (a), dark-field (b) images and SAED (c) from HPT-W. Similar to Fig. 2, notice the high density of defects in the grains, and break-ups in the elongated grains. The SAED shows nearly continuous rings, with no obvious intensity concentration along the rings, again indicating large-angle GBs. The HPT nominal equivalent strain in the specimen is around 70.

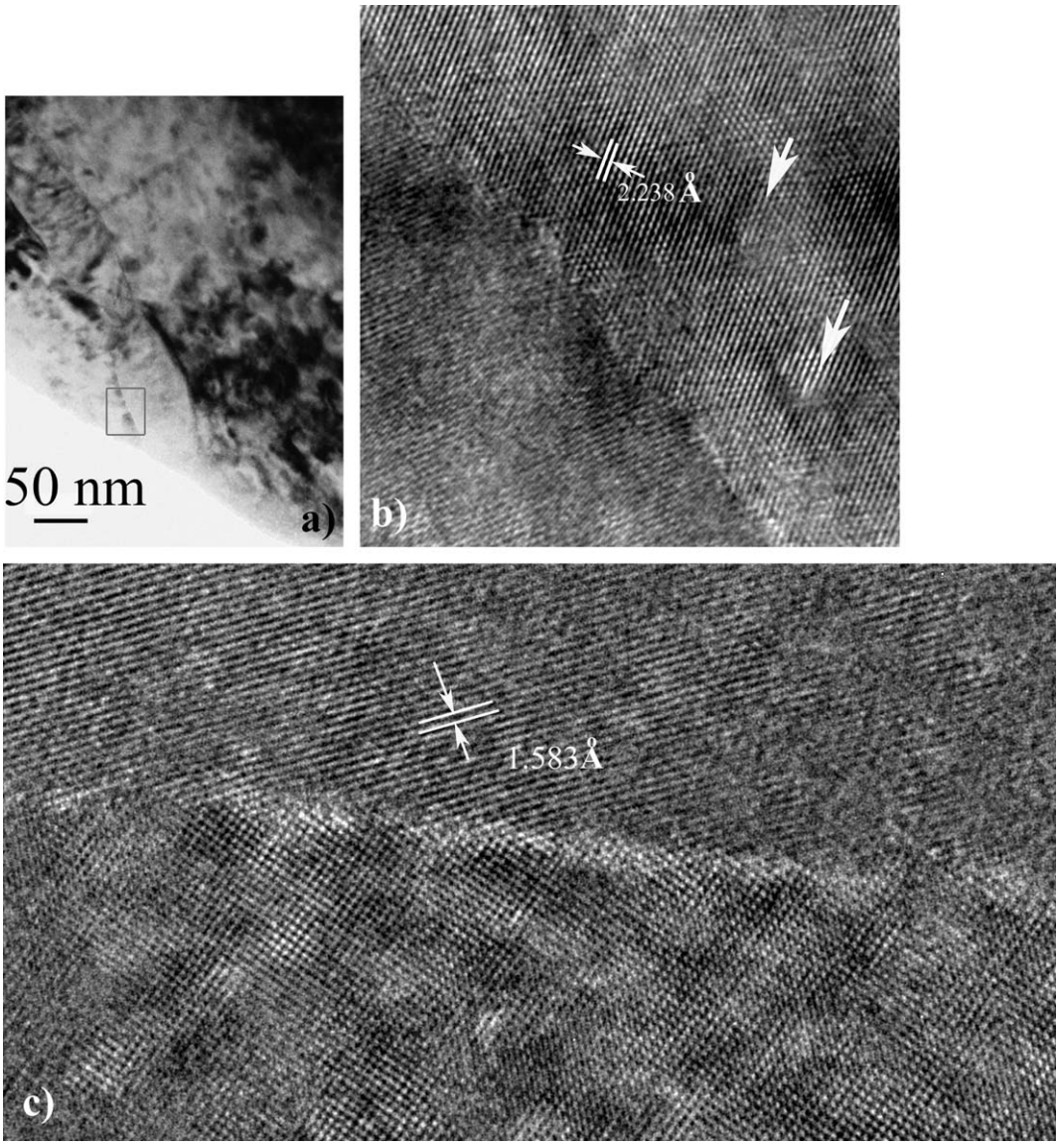


Fig. 4. Bright-field digital TEM image of HPT-W showing grains and grain boundaries (a). The GB region in the rectangular box in (a) is examined via lattice imaging, with the result presented in (b), where it is observed that the GB is of large angle, clean, well defined and has atomic steps. Edge dislocations are indicated by the extra-half atomic planes (the two white arrowed line guides). Another example of such large-angle, non-equilibrium GB is displayed in (c), where atomic steps or ledges are apparent.

amorphous GB region or GB phase can be identified as assumed in numerous models or simulations (e.g., Ref. [23]). Atomic steps and/or ledges exist along the GB, suggesting that such a GB is of a non-equilibrium and high-energy nature. Another observation is the residual edge dislocations, as indicated by the extra half atomic planes in the lattice image. It is of considerable significance to observe edge dislocations at room temperature in bcc metals such as W. This is because the rate-controlling factor for plastic deformation of bcc metals at low temperature ($T < 0.25T_m$) is the low mobility of screw dislocations; usually only straight screws are observed for single-crystal bcc metals after finite plastic deformation [24,25]. Fig. 4(c) shows another HRTEM micrograph showing a GB. Again, the GB is clean, atomically sharp and of the large-angle type. We can also observe atomic steps and ledges, suggesting the non-equilibrium nature of the GB. Such large-angle, non-equilibrium and high-energy GBs, along with large density of dislocations, are the common features of microstructures produced by SPD [7,26,27]. Valiev et al. argued that the "paradox" of strength and ductility of some UFG/nc metals and alloys may be explained by these features [7,27–29]. The large-angle, non-equilibrium GBs created during SPD can facilitate deformation mechanisms other than glide of dislocations. Such mechanisms include GB sliding and grain rotation [29]. The ledges or atomic steps along such non-equilibrium GBs can also act as dislocation sources under stress [30]. Combined with the SPD-induced mobile dislocations, they will also contribute to improve the ductility of the UFG/nc metal.

The break-ups and high density of defects in the elongated grains at least partly explain the discrepancy between the XRD grain size (or coherent domain size) and the TEM observations, since such will contribute to the broadening of the XRD peaks and lead to a much reduced coherent domain size based on XRD data. We should point out that due to the elongated geometry of the W grains it is difficult to give an accurate TEM measurement of the grain size and its distribution for the HPT-W.

### 3.2. Quasi-static and dynamic mechanical properties of HPT-processed nc-W

First, we measured the Vickers hardness on both the top and bottom faces of the HPT-W disk across the diameter. Fig. 5 displays the results as a function of the distance from the disk center. It shows that the hardness of the center is lower than that of the disk edge because of the lower strain at the center. However, the distribution of the hardness is not very inhomogeneous, particularly for the top part of the disk. Hardness values are about 11 GPa close to the disk edge. This impressively high hardness for a transition metal is comparable to some hard ceramics (the hardness of most sintered ceramics, such as silicon nitride, is about 20 GPa [31]). The Hall–Petch relation for W in terms of Vickers hardness is [32]

$$H = H_0 + K_H \cdot d^{-1/2} \quad (2)$$

where $H_0$ is 350 kg/mm$^2$, and $K_H$ is 10 kg/mm$^2$. Using the data in Fig. 5, we estimate the grain size of HPT-W to be around 170 nm close to the disk edge. This estimate agrees roughly with the TEM observations.

Hardness results suggest that HPT-W is super-strong, particularly at the disk edge. Fig. 6 shows the quasi-static uniaxial compressive stress–strain curves of HPT-W. The specimens are cut from different regions of the HPT disk to check the homogeneity of the mechanical properties.

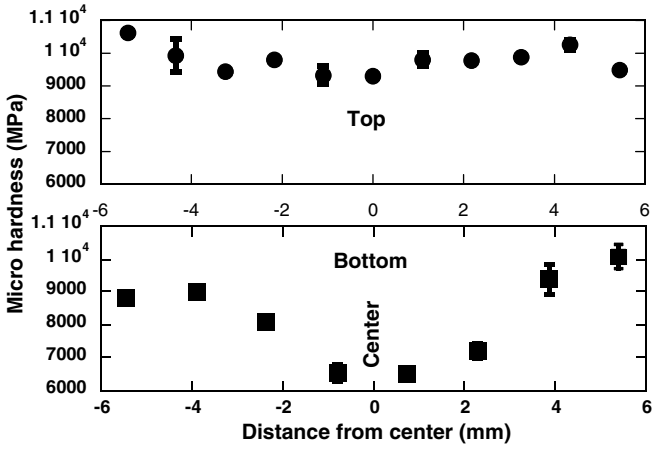


Fig. 5. Microhardness measurement on top and bottom faces of the HPT-W disk as a function of the distance from the disk center (mm). Notice the unusually high hardness (close to 11 GPa close to the disk edge, comparable to the hardness of some ceramics).

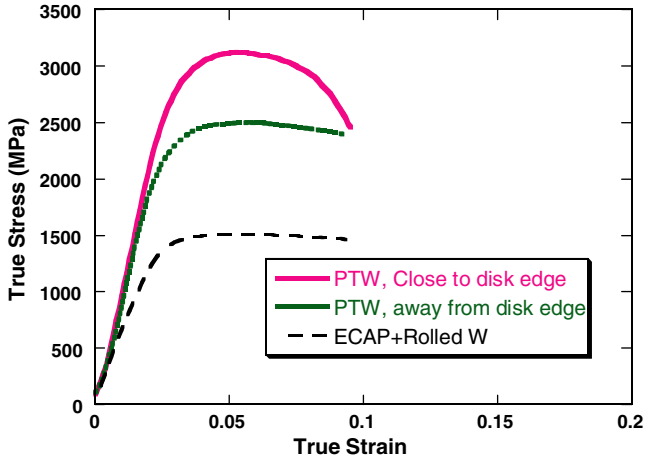


Fig. 6. Quasi-static uniaxial compression stress–strain curves. For the specimen cut from the disk edge (red, solid curve), the apparent loss of strength is most probably due to buckling of the specimen. For comparison, the stress–strain curve of a W specimen with UFG microstructure processed by ECAP and low-temperature rolling (ECAP + Rolled W in the plot) is also displayed. The flow stress of the disk-edge specimen is unusually high for a transition metal. The quasi-static compression result is in accordance with the microhardness measurement (Fig. 5). The flow stress is lower away from the disk edge, but is still much higher than that of the UFG-W.

The disk edge shows a flow stress as high as 3100 MPa, consistent with the hardness measurement (approximating the Vickers hardness number as roughly three times the yield stress [33]). This is a truly remarkable strength for tungsten. Away from the disk edge, the material becomes less strong, again in accordance with the hardness results. However, it is still stronger than a W sample that has a UFG microstructure (grain size $< 500$ nm) processed by ECAP and low-temperature rolling [15,16]. For comparison, the stress–strain curve for such a UFG-W is also included in Fig. 6. Due to the small dimension of the HPT-W specimen, it was difficult to maintain the axial alignment of the specimen with respect to the loading axis during compression. The presumable misalignment and the consequent buckling of the specimen might be responsible for the softening collapse of the flow stress in the strongest sample.

Fig. 7 displays the dynamic uniaxial stress–strain curves of various HPT-W specimens. The uniaxial dynamic compression tests were performed using a DTKB system (Fig. 1), allowing us to test samples with very small dimensions at high loading rates. These stress–strain curves show that HPT-W is very strong under these high loading rates (inertial effects are small for these samples, using the estimates of Ref. [18], as shown subsequently). Another important observation from these stress–strain curves is the precipitous stress collapse shortly after yielding. This stress collapse strongly suggests softening mechanisms taking place during dynamic loading. One definite softening mechanism stems from the adiabatic temperature rise during the course of dynamic loading, which can be calculated as

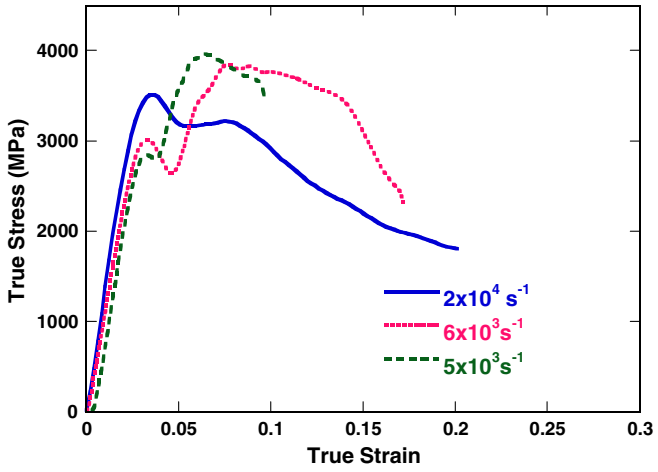


Fig. 7. Uniaxial dynamic stress–strain curves of HPT-W from DTKBar testing. Note the sharp stress collapse after dynamic yielding, which is desirable for some critical applications. Such stress collapse occurs much earlier than UFG-W [15,16].

$$\Delta T = \frac{\beta}{\rho C_P}\int_0^{\varepsilon_f} \sigma \, d\varepsilon \tag{3}$$

where $\beta$ is the Taylor–Quinney coefficient that characterizes the portion of plastic work converted into heat (assumed to be 0.9 in this case [34]), $\rho$ is the density (19.25 g/cm$^3$ for W), $C_P$ is the specific heat (0.134 J/g K for W [13]), $\sigma$ is the flow stress and $\varepsilon_f$ is the prescribed strain for the calculation (the prescribed strain is determined by the dimension and mass of the impacting projectile, the dimension of the specimen and the gas-gun pressure (or the velocity of the projectile), which are predetermined before the test). Assuming an elastic–perfect plastic isothermal stress–strain behavior with a strength $\sigma_y$ for the HPT-W, Eq. (3) can be written as

$$\Delta T = \frac{\beta}{\rho C_P}\sigma_y \cdot \varepsilon_f \tag{4}$$

For example, for a plastic strain of ~0.15, the temperature rise in the HPT-W under dynamic loading is around ~180 °C using a flow stress of ~3.5 GPa. Either for single-crystal W [35] or for severely plastically deformed W such as a ribbon from cold rolling [36], such a temperature rise may lead to considerable strength reduction. However, for single-crystal W, this strength reduction can be compensated for by strain hardening, whereas such compensation mechanism is absent in the SPD-W.

The stress wave loading during high strain rate experiments renders inertia effect a concern during the development of the DTKB technique [18]. The following equation has been derived to assess the relative error in flow stress measurement due to inertia [18]:

$$\frac{\sigma_{s,2} - \sigma_y}{\sigma_y} = \frac{\rho d^2}{\sigma_y}\left[\frac{1}{64} + \frac{1}{6}\left(\frac{l}{d}\right)^2\right]\dot{\varepsilon}^2 \tag{5}$$

where $\sigma_{s,2}$ is the measured flow stress, $\sigma_y$ is the actual flow stress, $\rho$ is the density of the material, $l$ is the length and $d$ is the diameter of the specimen, and $\dot{\varepsilon}$ is the strain rate. Eq. (5) shows that tests on materials with high flow stress and low density are less prone to such inertial errors, while very high density materials and very soft materials will be susceptible to inertial effects. Estimates based on Eq. (5) and our experimental results (the equivalent aspect ratio $l/d$ of our specimens is ~0.8) indicate that even though tungsten is a material of high mass density, the super-high strength of HPT-W off-sets its effect and results in a reasonably accurate measurement of its dynamic strength using the DTKB technique.

The salient early precipitous stress collapse in the uniaxial dynamic stress–strain curves is a desirable feature for

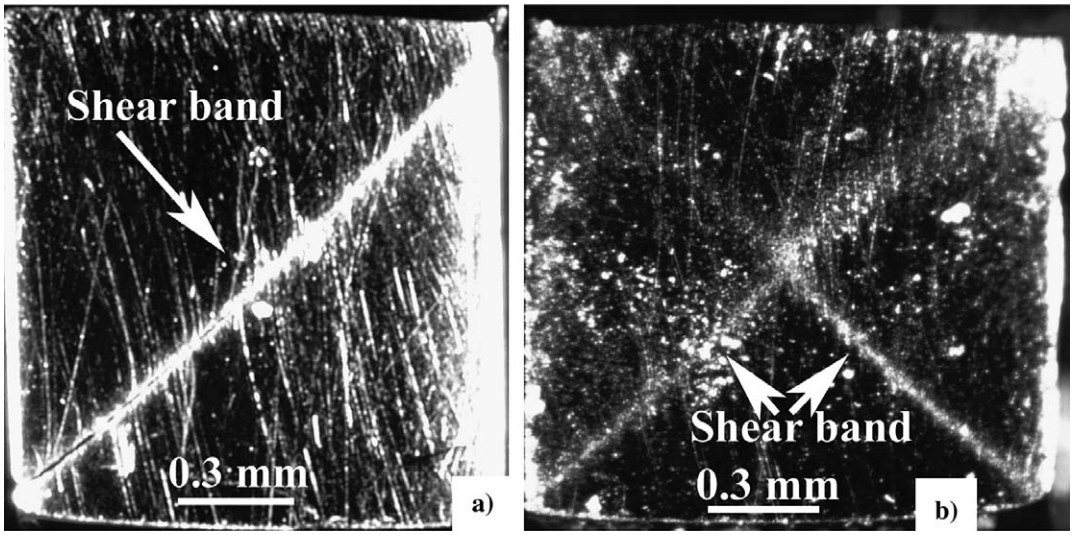


Fig. 8. Post-mortem optical images. Localized shearing resulted in the formation of a major shear band and subsequent cracking of the dynamically loaded HPT-W (a), and formation of two intersecting shear bands (b). The shear bands are at an angle of about 45° with respect to the loading direction (horizontal in both (a) and (b)). The loading direction is along the disk plane normal.

some critical applications such as anti-armor kinetic energy penetrators [37]. Usually such stress collapse is a result of localized plastic deformation in the form of adiabatic shear banding. Fig. 8 shows post-loading optical images of HPT-W dynamic testing specimens. Fig. 8(a) displays a single shear band, while Fig. 8(b) displays the development of two intersecting shear bands. The loading directions in both figures are horizontal, and normal to the disk plane. The shear bands subtend an angle of approximately 45° with respect to the loading direction. Fig. 9(a) displays an SEM image of the surface of a dynamically loaded HPT-W. The bright contrast running from the lower left corner to the upper right corner of the image indicates localized shearing. The boundary of the shear region is not very sharp. No crack is observed due to the small prescribed strain. Fig. 9(b) shows an SEM micrograph of another dynamic specimen. Here we observe a shear band, and the subsequent crack. The severe localized shear flow is indicated by the bending of the pre-existing scratches near the crack. (Those scratches were introduced during sample preparation.) The width of the adiabatic shear band of HPT-W is only about 5 μm, much smaller than that of UFG-W. (Fig. 9(c) displays the microstructure of an adiabatic shear band of a UFG-W. The shear band width is ~40 μm [15,16].)

Fig. 10(a) displays one half of a failed dynamic testing specimen. Clearly, the failure occurred as a consequence of severe localized shearing. The failure is similar to consolidated nanostructured Fe [38,39], nanostructured vanadium [40] and bulk metallic glasses [41]. In Fig. 10(b), an enlarged micrograph shows the localized shearing marks along the face normal to the fracture surface. Figs. 10(c) and (d) display the fracture surface of two different areas, indicating slightly different fracture modes. It is revealing to examine the fracture surface displayed by Figs. 10(c) and (d) in more detail. The patterns in Figs. 10(c) and (d) appear similar to those observed in the fracture surface of bulk metallic glasses where they are called river patterns [41]. (It has been asserted that in metallic glasses, shear banding is the only operational plastic deformation mechanism under mechanical straining [42].) In the case of HPT-W, however, the river exhibits a much rougher surface. The fronts of the waves are curved and irregular (Fig. 10(c)). Some step-like features about 5 μm in height are visible at higher magnifications (Fig. 10(d)) which are accompanied by dense, river-like patterns. All these suggest some plastic deformation before failure. The details and the underlying mechanisms for such fracture modes in nanocrystalline tungsten, or perhaps in nanocrystalline bcc metals in general, call for further investigations.

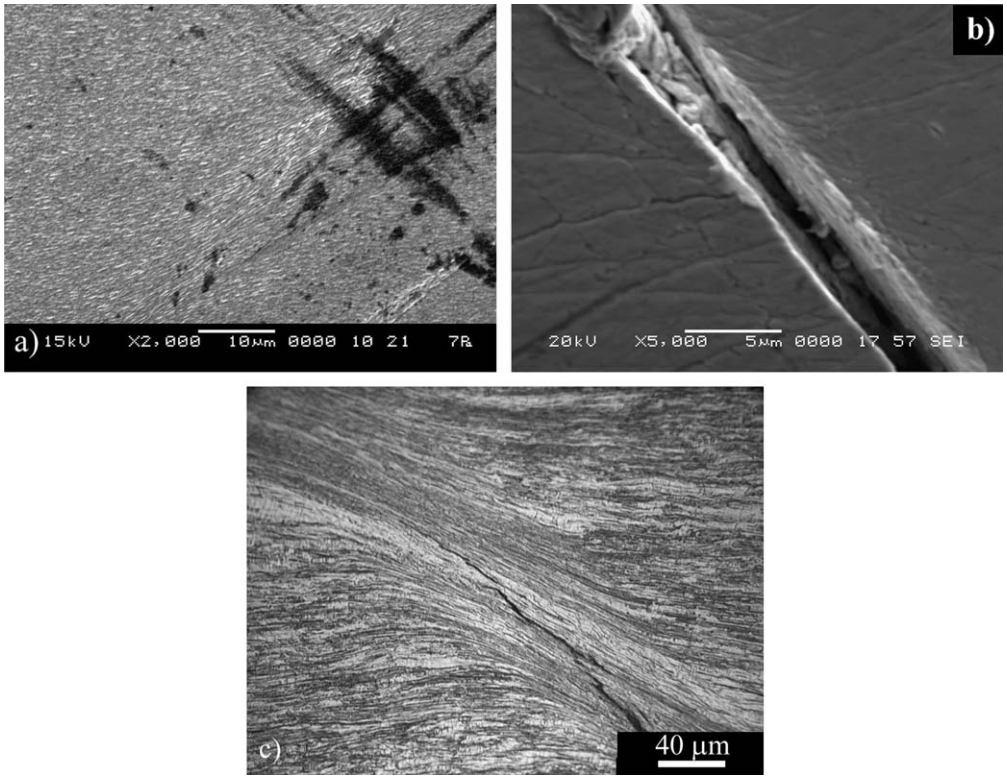


Fig. 9. (a) SEM image of dynamically loaded HPT-W showing the localized shearing (features in bright contrast running from the lower left corner to the upper right corner of the image); (b) SEM micrograph of adiabatic shear under dynamic compression of HPT-W, and subsequent cracking. (Note the severe localized shearing indicated by the bending of the pre-existing mechanical scratches introduced during sample preparation.) The width of the shear band is approximately 5 μm, much narrower than the shear band observed in UFG-W produced by ECAP and warm rolling (the shear band width of the UFG-W is ~40 μm, as displayed in (c)).

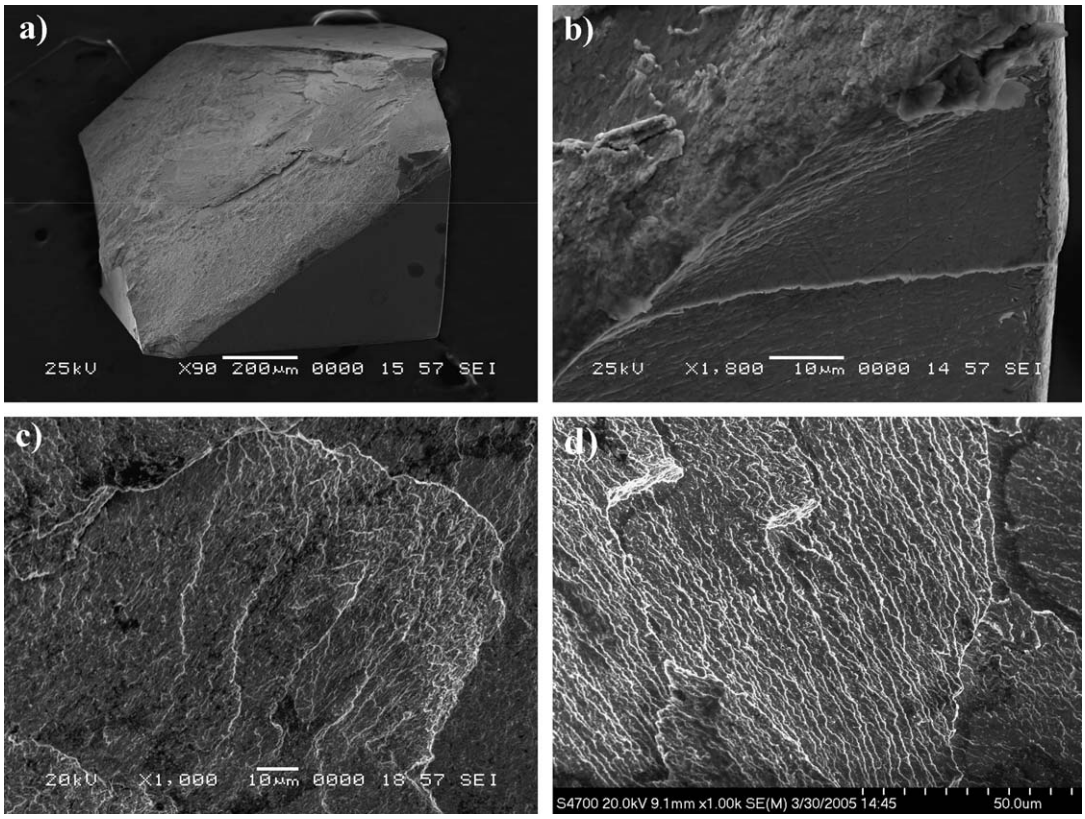


Fig. 10. One half of a dynamically failed HPT-W specimen showing the failure as a consequence of severe localized shearing (a). (b) The evidence of shearing close to the fracture surface is clear. (c and d) Two fracture surfaces are displayed. It is revealing to compare the fracture surfaces of (c) and (d) with those observed in metallic glasses which exhibit the so-called ''river pattern'' [41]. However, in the case of HPT-W, the river is much rougher with a much higher density of curved ripples than that of metallic glasses, indicating some ductile plastic flow before failure.

## 4. Discussion

Some abnormal phenomena have been observed in the mechanical behavior, particularly the plastic deformation of metals and alloys with UFG or nc microstructures [43]. One interesting observation is that when the grain size is refined into the UFG/nc regimes, the strain rate sensitivity of face-centered cubic (fcc) metals is increased, while that of bcc metals is decreased [44]. We have argued, based on the physics and mechanics of adiabatic shear banding in metals and alloys, that combined with much elevated flow stress and the elastic–nearly plastic behavior of bcc metals with UFG/nc microstructures, such reduced strain rate sensitivity will promote the tendency to adiabatic shear localization under dynamic loading [15,16,45]. The experimental results presented in this paper attest to this general theory.

Intergranular fracture is the predominant fracture mode for polycrystalline W, as well as for Cr and Mo that belong to the same group of the periodical table as W (group VIA) [46,47]. Some investigators regard such behavior more or less intrinsic to these metals from a survey of the ratio of the shear moduli to the bulk moduli ($\mu/K$, $\mu$ being the shear modulus and $K$ the bulk modulus), the postulation being that the intrinsic brittleness of a metal or metallic material is correlated to this ratio [41,48]. For example, most ductile metals, especially those in the fcc family, have low values of $\mu/K$ ($\sim$0.3 or below; 0.123 for Au, perhaps the most ductile metal) while those in the bcc family, particularly Cr, Mo and W, have much higher values of $\mu/K$ (>0.5). However, the fact that single-crystal W can be deformed to large plastic strains even at liquid nitrogen temperature [35] suggests that the brittle behavior of W is not intrinsic. In fact, the major cause for the intergranular fracture in polycrystalline W is the segregation of the solvable interstitial atoms along the GBs, which makes the GBs become weak links under mechanical straining. This is consistent with the unusually high GB energy in pure polycrystalline W (>1000 mJ/m$^2$, compared to 340 mJ/m$^2$ in Au), as it renders the GBs in W the favored sites for interstitial segregation. In view of this, GB engineering [49] may be used to improve the mechanical behavior of such metals. For contamination free GBs in pure metals, low-angle GBs are more fracture resistant than large-angle ones based on a simple energetic argument. The problem becomes more complicated when impurity segregation along the GBs is involved. There have been long-standing efforts in using GB engineering to improve the fracture resistance of metals [50]. However, the possibility of modifying the GB structure into one that is more resistant to GB embrittlement caused by segregation

has been little exploited. In our previous work on UFG-W, we observed substantial improvement in the ductility of W due to the plastic deformation induced grain refining [15,16]. Under either quasi-static or uniaxial dynamic compression, cg-W exhibits axial cracks [51,52]. However, experimental results in the present work on HPT-W show only localized shearing and subsequent cracking or failure under dynamic compression. The dynamic failure mode bears some similarity to that of metallic glasses, i.e., appearance of river pattern, but with a much rougher morphology indicative of some ductile feature associated with the dynamic failure process. No axial cracking was observed in the quasi-statically compressed HPT-W specimens. These observations are in accordance to our previous experimental results on UFG-W processed by SPD and imply that the HPT-W has enhanced ductility compared to the conventional cg-W. Systematic work by Gumbsch et al. [12] on controlling factors for the fracture toughness and brittle-to-ductile transition in single-crystal W indicates that pre-plastic deformation of the specimen can increase both low- and high-temperature fracture toughness. In particular, much improved high-temperature fracture toughness is achieved by pre-plastic deformation. Gumbsch et al. pointed out that if a dislocation (either one that is generated at the crack tip or a pre-existing one) moves in the stress field along the crack tip, it will generate dislocation segments of non-screw (and thus highly mobile) character parallel to the crack tip. Our HRTEM analysis shows residual edge dislocations in the HPT nc-W (Fig. 4(b)). Such edges may work together with other pre-existing mobile dislocation components so as to provide highly efficient shielding of the crack tip, thus resulting in relatively ductile failure.

The effect of grain size on strength and ductility of metals has been a controversial issue. Usually, when the strength of a metal is increased by grain size reduction (Hall–Petch strengthening), the ductility measured by elongation to failure during a tensile test is reduced. Following the instability criteria [53], the major reason for this is the reduction of the stabilizing mechanism due to the reduced strain hardening associated with grain size refinement [54]. However, recent research has shown that judicious microstructure engineering can produce nc/UFG metals with concurrent high strength and ductility. One approach is the bi-modal grain size distribution [55,56] where the nc grains strengthen the microstructure while the large grains (grain size in micrometer range) sustain the high ductility. Especially for nc/UFG metals processed by SPD, Valiev et al. [29,57] proposed that recourse to the nature of the GBs generated during such processing can explain the strength/ductility paradox of nc/UFG metals. In this work particularly, both conventional and HRTEM results suggest that the GBs in HPT-W are of large angle and a high-energy and non-equilibrium nature. Such GBs should serve as ideal attracting sites for interstitial impurities present along the pre-existing GBs. Disruption of the structure and chemistry of the pre-existing GBs during SPD might have contributed to this redistribution process, which renders the GBs less contaminated by the detrimental impurities. In addition to these beneficial effects, the remnant edge dislocations revealed by HRTEM (Fig. 4(b)) may also help to enhance the ductility of the nc-W, as briefly discussed previously.

## 5. Summary and concluding remarks

We have investigated the microstructure and mechanical properties, particularly the GB structure and the mechanisms of plastic deformation and failure under dynamic loading, of a fully dense nc-W processed by HPT. We have come to the following findings from our experimental results and discussions:

(1) The fully dense nc-W exhibits remarkably high strength (hardness ~11 GPa close to the disk edge, strength ~3.0 GPa under quasi-static and ~4.0 GPa under dynamic compression).
(2) While the grains have an elongated geometry, breakups and high density of dislocations are observed within the grains. SAED does not show strong texturing.
(3) The grain boundaries in the nc-W are mostly of large-angle type. HRTEM shows that the GBs are clean, well-defined (atomically sharp) with some atomic steps and ledges, indicating that the GBs are of a non-equilibrium and high-energy nature. We also observed edge dislocations within the grains with HRTEM.
(4) While the nc-W has mechanical strength comparable to that of some strong ceramics, its quasi-static and dynamic failure is not completely brittle. Under uniaxial dynamic compression, the specimens exhibit localized shearing, similar to their UFG counterparts processed by ECAP plus cold rolling [15,16], and to many other bcc metals with UFG/nc microstructures [39,40]. The shear band width in the HPT-processed nc-W is ~5 μm, much smaller than that of the UFG-W (~40 μm).
(5) The dynamic failure surface exhibits river patterns akin to that of metallic glasses. But the river surface is much rougher, with more curved and irregular morphology than that of metallic glasses, suggesting ductile plastic deformation before final failure. However, we point out that further effort is needed to clarify the dynamic failure mechanism of nanocrystalline metals, especially those with bcc structure.

## Acknowledgements

The authors thank Dr. T.W. Wright and Dr. J. McCauley (US Army Research Laboratory), and Professor E. Ma (Johns Hopkins University) for helpful discussions. This work was performed at JHU-CAMCS, sponsored by

ARL under the ARMAC-RTP Cooperative Agreement #DAAD19-01-2-0003.

## References

[1] Gleiter H. Prog Mater Sci 1989;33:223–315.
[2] Gleiter H. Acta Mater 2000;48:1–29.
[3] Suryanarayan C. Int Mater Rev 1995;40:41–63.
[4] Erb U, Aust KT, Palumbo G. In: Koch CC, editor. Nanostructured materials. Noyes; 2002.
[5] Groza JR. In: Koch CC, editor. Nanostructured materials. Noyes; 2002.
[6] Lowe TC, Valiev RZ, et al. Investigations and applications of severe plastic deformation. Kluwer Academic; 2000.
[7] Valiev RZ, Islamgaliev RK, Alexandrov IV. Prog Mater Sci 2000;45:103–89.
[8] Tao NR, Wang ZB, Tong WP, Sui ML, Lu J, Lu K. Acta Mater 2002;50:4603–16.
[9] Zhilyaev AP, Nurislamova GV, Kim B-K, Baro MD, Szpunar JA, Langdon TG. Acta Mater 2003;51:753–65.
[10] Valiev RZ, Ivanisenko YV, Rauch EF, Baudele B. Acta Mater 1996;44:4705–12.
[11] Zhilyaev AP, Lee S, Nurislamova GV, Valiev RZ, Langdon TG. Scr Mater 2001;44:2753–8.
[12] Gumbsch P, Riedle J, Hartmaier A, Fischmeister HF. Science 1998;282:1293–5.
[13] Lassner E, Schubert W-D. Tungsten: properties, chemistry, technology of the element, alloys and chemical compounds. Kluwer Academic/Plenum; 1998.
[14] Allen BC, Maykuth DJ, Jaffee RI. J Inst Met 1961;90:120–8.
[15] Wei Q, Ramesh KT, Ma E, Kesckes LJ, Dowding RJ, Kazykhanov VU, et al. Appl Phys Lett 2005;86:101907.
[16] Wei Q, Jiao T, Ramesh KT, Ma E, Kecskes LJ, Magness L, et al. Acta Mater 2006;54:77–87.
[17] Alexandrov IV, Raab GI, Shestakova LO, Kil'mametov AR, Valiev RZ. Phys Metals Metall 2002;93:493–500.
[18] Jia D, Ramesh KT. Exp Mech 2004;44:445–54.
[19] Farrell K, Schaffhauser AC, Stiegler JO. J Less-common Met 1967;13:141–55.
[20] Keijser THD, Langford JI, Mittemeijer EJ, Vogels ABP. J Appl Crystallogr 1982;15:308–14.
[21] Follansbee PS. ASM metals handbook, vol. 8. Materials Park (OH): American Society of Metals; 1985. p. 190.
[22] Jiang HG, Ruhle M, Lavernia EJ. J Mater Res 1999;14:549–59.
[23] Jiang B, Weng GJ. Metall Mater Trans A 2003;34:765–71.
[24] Christian JW. Metall Trans A 1983;14:1237.
[25] Keh AS, Weissmann S. In: Thomas G, Washburn J, editors. Electron microscopy and strength of crystals. New York (NY): Interscience; 1963. p. 231.
[26] Nazarov AA, Romanov AE, Valiev RZ. Acta Metall Mater 1993;41:1033–40.
[27] Valiev RZ, Korznikov AV, Mulyukov RR. Mater Sci Eng A 1993;168:141–8.
[28] Valiev RZ. Nature Mater 2004;3:511–6.
[29] Valiev RZ, Alexandrov IV, Zhu YT, Lowe TC. J Mater Res 2002;17:5–8.
[30] Li JCM. Trans Metall Soc AIME 1963;227:239–47.
[31] Blau PJ, Martin RL, Zanoria ES. Wear 1997;203:648–57.
[32] Vashi UK, Armstrong RW, Zima GE. Metall Trans 1970;1:1769–71.
[33] Tabor D. The hardness of metals. Oxford: Clarendon Press; 1951.
[34] Bai Y, Dodd B. Adiabatic shear localization. Oxford: Pergamon Press; 1992.
[35] Argon AS, Maloof SR. Acta Metall 1966;14:1449–62.
[36] Boser O. J Less-common Met. 1971;23:427–35.
[37] Wright TW. The physics and mathematics of adiabatic shear bands. Cambridge University Press; 2002.
[38] Jia D, Ramesh KT, Ma E. Acta Mater 2003;51:3495–590.
[39] Wei Q, Jia D, Ramesh KT, Ma E. Appl Phys Lett 2002;81:1240–2.
[40] Wei Q, Jiao T, Ramesh KT, Ma E. Scr Mater 2004;50:359–64.
[41] Lewandowski JJ, Wang WH, Greer AL. Philos Mag Lett 2005;85:77–87.
[42] Argon AS. Acta Metall 1979;27:47–58.
[43] Kumar KS, Van Swygenhoven H, Suresh S. Acta Mater 2003;51:5743–74.
[44] Wei Q, Cheng S, Ramesh KT, Ma E. Mater Sci Eng A 2004;381:71–9.
[45] Wei Q, Kecskes LJ, Jiao T, Hartwig KT, Ramesh KT, Ma E. Acta Mater 2004;52:1859–69.
[46] Brosse JB, Fillit R, Biscondi M. Scr Mater 1981;15:619–23.
[47] Thornley JC, Wronski AS. Scr Mater 1969;3:935–8.
[48] Hecker SS, Rohr DL, Stein DF. Metall Trans A 1978;9:481–8.
[49] Watanabe T. Res Mech 1984;11:47–84.
[50] Hirth JP. Metall Trans 1972;3:3047–66.
[51] Dummer T, Lasalvia JC, Ravichandran G, Meyers MA. Acta Mater 1998;46:6267–90.
[52] Lennon AM, Ramesh KT. Mater Sci Eng A 2000;276:9–21.
[53] Hart EW. Acta Metall 1967;15:351–5.
[54] Gil Sevillano J, Arizcorreta IO, Kubin LP. Mater Sci Eng A 2001;309–310:393–405.
[55] Ma E. Scr Mater 2003;49:663–8.
[56] Wang YM, Chen MW, Zhou FH, Ma E. Nature 2002;419:912–5.
[57] Valiev RZ, Gertsman VY, Kaibyshev R. Phys Stat Sol A 1986;97:11–56.